

Precise Robot-Assisted Guide Positioning for Distal Locking of Intramedullary Nails

Ziv Yaniv*, Member, IEEE, and Leo Joskowicz, Senior Member, IEEE

Abstract—This paper presents a novel image-guided robot-based system to assist orthopedic surgeons in performing distal locking of long bone intramedullary nails. The system consists of a bone-mounted miniature robot fitted with a drill guide that provides rigid mechanical guidance for hand-held drilling of the distal screws' pilot holes. The robot is automatically positioned so that the drill guide and nail distal locking axes coincide, using a single fluoroscopic X-ray image. Since the robot is rigidly attached to the intramedullary nail or bone, no leg immobilization or real-time tracking is required. We describe the system and protocol and present a method for accurate and robust drill guide and nail hole localization and registration. The *in vitro* system accuracy experiments for fronto-parallel viewing show a mean angular error of 1.3° (std = 0.4°) between the computed drill guide axes and the actual locking holes axes, and a mean 3.0 mm error (std = 1.1 mm) in the entry and exit drill point, which is adequate for successfully locking the nail.

Index Terms—Fluoroscopic X-ray, pose-estimation, robot guidance.

I. INTRODUCTION

COMPUTER INTEGRATED SURGERY (CIS) systems can potentially benefit many orthopedic surgical procedures. Indeed, a few dozen CIS systems for orthopedic procedures are currently deployed [1].

Our work focuses on a technique for fracture reduction called closed intramedullary nailing. Closed intramedullary nailing is currently the routine procedure of choice for reducing fractures of the femur and the tibia [2]. It restores the integrity of the fractured bone by means of a nail inserted in the medullary canal. The nail is inserted without surgically exposing the fracture through an opening, usually in the proximal part of the bone. The surgeon reduces the fracture by manipulating the proximal and distal bone fragments through the leg until they are aligned. The surgeon then inserts a guide wire, reams the canal if necessary, and drives the nail in. In most cases, the surgeon also inserts lateral proximal and distal interlocking screws to prevent fragment rotation and bone shortening. The procedure is per-

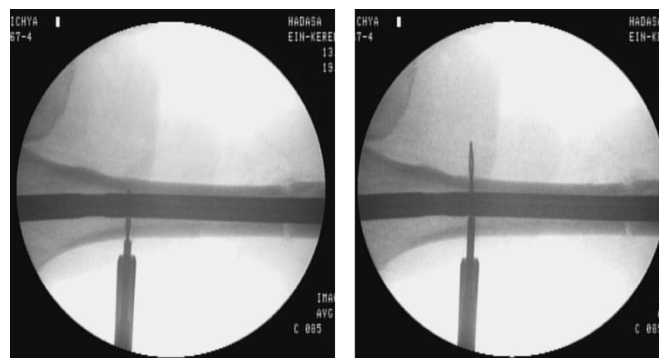


Fig. 1. Fluoroscopic X-ray anterior-posterior images acquired during pilot hole drilling.

formed under X-ray fluoroscopy, which is used to view the position of bone fragments, surgical tools, and implants. Numerous fluoroscopic X-ray images are required, especially during distal locking [3].

Distal locking—the insertion of lateral screws to prevent nail rotation—has long been recognized as one of the most challenging steps in this procedure. Since the nail deforms by several millimeters to conform to the bone canal shape, the exact position of the distal locking nail holes' axes cannot be determined in advance. By repeatedly alternating between anterior-posterior and lateral fluoroscopic X-ray views, the surgeon adjusts the entry point and orientation of the drill so that its axis coincides with the corresponding nail hole axis. Drilling proceeds incrementally, with each advance verified with a new pair of fluoroscopic X-ray images (Fig. 1). Once the pilot hole passing through the distal locking nail's hole has been drilled, the locking screw is fastened. Complications include inadequate fixation, malrotation, bone cracking, cortical wall penetration, and bone weakening due to multiple or enlarged pilot holes. The literature reports that the surgeon's direct exposure to radiation per procedure without the use of CIS systems is 3–30 min, of which 31%–51% is spent on distal locking depending on the patient anatomy and the surgeon's skill [3].

We have developed a novel image guided robot-based system for distal locking. The system consists of a bone-mounted miniature parallel robot [4] fitted with a drill guide that provides precise rigid mechanical guidance for hand-held drilling of the distal screws' pilot holes. The robot is automatically positioned so that the drill guide and nail distal locking axes coincide using a single fluoroscopic X-ray image [5]. In this paper, we describe the system and present methods for accurate and robust drill guide and nail hole localization and registration and report the results of *in vitro* system accuracy experiments.

Manuscript received March 31, 2004; revised December 1, 2004. This work was supported by grants from the Israel Ministry of Industry and Trade, the IZMEL Consortium on Image-Guided Therapy, and by the Israel Ministry of Science and Technology. The Associate Editor responsible for coordinating the review of this paper and recommending its publication was P. Cinquin. Asterisk indicates corresponding author.

*Z. Yaniv is with the Imaging Science and Information Systems (ISIS) Center, Department of Radiology, Georgetown University Medical Center, 2115 Wisconsin Ave., Suite 603, Washington, DC 20007 USA (e-mail: zivy@isis.imac.georgetown.edu).

L. Joskowicz is with the School of Computer Science and Engineering, The Hebrew University of Jerusalem, Jerusalem 91904 Israel (e-mail: josko@cs.huji.ac.il).

Digital Object Identifier 10.1109/TMI.2005.844922

II. PREVIOUS WORK

Many non-CIS devices have been developed for distal locking. Examples include proximally mounted targeting devices [3], stereo fluoroscopy [6], and mechanical guides [7]. However, all of these devices and their associated techniques have deficiencies: they are only selectively applicable, are cumbersome and difficult to use, or are not sufficiently accurate and, thus, fail to significantly reduce the likelihood of patient complications.

Fluoroscopy-based CIS navigation systems [8]–[10] take the guesswork out of targeting. The systems enhance, reduce, or altogether eliminate fluoroscopic X-ray images by replacing them with a virtual reality view in which the bone and instruments' positions are continuously updated and viewed on-screen as they move. They help the surgeon align the drill axis with the distal locking nail hole axis to an accuracy of about 1 mm and 1° . However, they do not provide a mechanical guide for the hand-held drill, which can slip or deviate from its planned trajectory at the entry point and during the drilling. Thus, the surgical outcomes are still largely dependent on the surgeon's skill.

A CIS system for distal locking which combines a passive mechanical aiming device, an optical navigation system and fluoroscopic images is described in [11]. In this system, the drilling axes are computed from the fluoroscopic X-ray images of the nail and the fiducials that are mounted on the passive mechanical aiming device. The surgeon then manually orients the aiming device under guidance of the optical navigation system. Once the desired pose is attained, the aiming device is locked in place and the pilot holes are drilled. The two main differences between our system and this system are: 1) our system automatically positions a robot to align the drill guide, while this system relies on manual alignment guided by an optical navigation system, and; 2) our system remains registered throughout the procedure regardless of patient movement, while this system requires re-registration. Mounting the robot directly onto the patient enables us to perform a single registration which is valid throughout the procedure.

Robot-based CIS systems are designed to assist the surgeon in implementing the preoperative plan by mechanically positioning and sometimes executing the surgical action itself [12], [13]. The robots are either modified floor-standing industrial robots, or table-mounted custom-designed serial robots. They are usually voluminous and heavy although they have relatively small workloads and work volumes. In these systems, bone immobilization or real-time dynamic tracking is required, since the relative location of the bone with respect to the robot must be known precisely at all times. This complicates the registration procedure and adversely affects the overall system accuracy.

Fluoroscopic image guidance of robotic systems can be divided into two categories: 1) open loop calibrated guidance [14], [15], and; 2) closed loop un-calibrated guidance [16]–[18]. Open loop calibrated guidance methods compute the robot's spatial localization with respect to the camera coordinate system by imaging a target with known geometry. The desired robot pose is then specified, either automatically

or manually, in the camera coordinate system and the robot is aligned accordingly. Since the internal camera parameters are required for robot pose estimation, the C-arm must be calibrated. Closed loop un-calibrated methods guide the robot to the desired pose based solely on the acquired images. The desired target pose is specified, either automatically or manually, in the image coordinate system. The robot pose is then updated continuously according to the images, until the desired pose is attained.

We opt for an open loop calibrated method, as do [14] and [15], because it requires significantly fewer fluoroscopic X-ray images and, thus, minimizes patient exposure to harmful radiation and reduces intraoperative time. The main difference between these systems and ours is in the definition of the robot target pose. Both of these systems require the acquisition of a computed tomography (CT) scan on which the target pose is defined preoperatively. The CT scan is then registered to the intraoperative situation using either 2-D/3-D fluoroscopic X-ray to CT registration or 3-D/3-D contact based registration. This defines the robot target pose intraoperatively. Our system does not require a CT scan and only uses the intraoperative fluoroscopic images to determine the robot target pose.

III. SYSTEM OVERVIEW AND PROTOCOL

The key concept of the proposed system is the automatic positioning of a mechanical targeting drill guide with respect to the intramedullary nail holes with a single fluoroscopic X-ray image. The drill guide is fitted to a miniature sterilizable robot which is directly mounted on the bone or on the nail's head, via a supporting plate, in the vicinity of the distal holes. The miniature robot serves as a fine positioning device whose precision and work volume is sufficient to realize the drilling and to achieve the desired accuracy. Because the robot forms a rigid body with the intramedullary nail and the bone, no leg immobilization or real-time tracking is necessary during surgery.

A. Materials

The system consists of the MARS sterilizable miniature robot [4], a robot mounting plate, a drill guide attached to the robot, an image calibration ring for the fluoroscopic X-ray unit, a PC computer with a video frame grabber, and image-based guidance software.

MARS is a $5 \times 5 \times 7 \text{ cm}^3$, 150-gram six-degree-of-freedom parallel manipulator whose work volume is about 10 cm^3 and whose accuracy is better than 0.1 mm. It is designed to operate in semi-active mode, that is, to position and orient the targeting guide to a precise predetermined location, and then lock itself in place to serve as a guide for manual targeting. When locked, it is rigid and can withstand forces of a few kilograms. The robot comes with a PC-based controller card that receives joint position feedback and calculates the inverse kinematics for joint-level control.

MARS is rigidly placed in the vicinity of the distal holes by either attaching it to the distal bone fragment or by attaching it to the intramedullary nail's head. Distal bone fragment mounting is done with two unicortical 4 mm screws drilled in the vicinity of the distal nail holes to which a robot mounting plate with

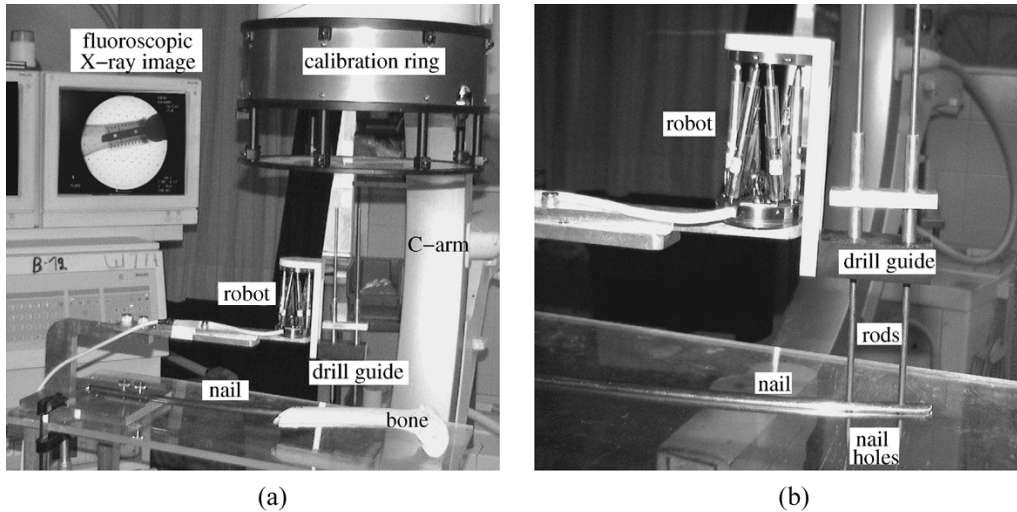


Fig. 2. Photographs of: (a) the *in vitro* setup and (b) the MARS robot in its desired configuration, where the drill guide and nail holes axes are aligned, as shown by the two rods passing through them.

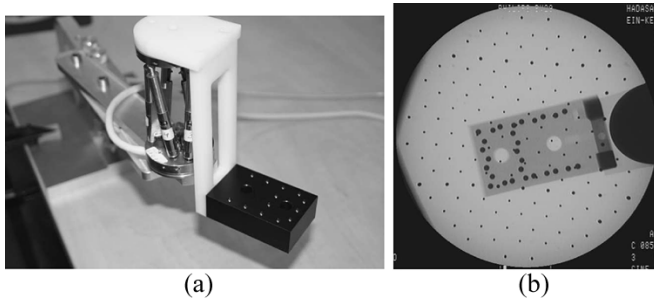


Fig. 3. (a) Photographs of the drill guide target mounted on robot and (b) its fluoroscopic X-ray image.

two snap-on pins is attached. Nail head mounting is done with a U-shaped adaptor that directly screws into the nail's head. The horizontal length of the plate, parallel to the bone axis, is adjustable to roughly match the nail's length [Fig. 2(a)]. Both options are minimally invasive. Previous work on spine fixation [19] and our limited experience with the intramedullary nail indicates that the concept is viable and that unless the bone is osteoporotic, the fixation is rigid.

The drill guide is directly mounted on the robot's upper base with a connecting arm. It is a $40 \times 55 \times 15$ mm³ Delrin radio-lucent block with two guiding holes 30 mm apart, which is the spacing between the nail holes. It has a pattern of 28 3-mm stainless-steel fiducial spheres asymmetrically distributed on two planes 20 mm apart that are used for its spatial localization [Fig. 3(a)].

The image calibration ring for the fluoroscopic X-ray unit is the FluoroTrax C-arm calibration ring (Traxtal, Canada). The PC and video frame grabber are off-the-shelf, standard, equipment.

B. Protocol

The surgical protocol is as follows. Once the fracture has been reduced and the nail has been inserted, the image calibration ring is mounted on the C-arm image intensifier. The surgeon then mounts the robot onto the patient, either directly onto the distal bone, or onto the nail head.

When the robot is mounted on the distal bone, the surgeon determines the approximate location of the two self-tapping uncortical screws onto which the robot base will be mounted based on a distal lateral fluoroscopic X-ray image. Their axes should be roughly parallel to the distal nail holes' axes and several centimeters proximal to them. The surgeon then drills, with a hand-held jig, two parallel pilot holes at 30-mm distance along the axis of the nail. The screws are then fastened and the robot base is affixed to them. When the robot is mounted on the nail head, one end of the U-shaped adaptor is directly screwed onto the nail's head. On the other end, the length of the support plate is adjusted according to the nail's length, and the robot is mounted on it. In both cases, the targeting drill guide is then mounted on the robot top base.

Next, the X-ray technician adjusts the orientation of the C-arm, under our software guidance, to achieve a fronto-parallel (FP) view in which the distal locking nail holes appear as circles (and not ellipses) in the image. This task is routine in the current procedure and typically requires 2–6 images. The software then estimates the required robot pose so that the drill guide axes and nail axes coincide. Alternatively, a single lateral fluoroscopic image is acquired and the required robot pose is computed from it. Once the robot is positioned and locked in place, the surgeon manually drills the pilot holes through the drill guide and places the distal locking screws. Finally, the surgeon removes the robot and completes the surgery according to the usual protocol.

C. Method

The most challenging computational task in the above procedure is the accurate and robust computation of the transformation that aligns the drill guide and the nail hole axes.

Localization of the nail holes and the drill guide is difficult because partial occlusions are inherent to the setup: the robot is mounted close to the nail holes and the image includes the nail, bone, and soft tissue. The nail holes are small (5-mm diameter, about 20 pixels), nearby (30 mm), and appear as ellipses in the images, so the accuracy with which their axes can be determined

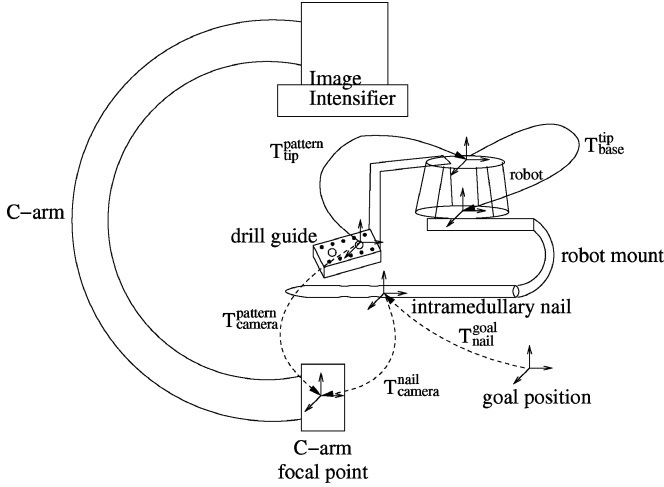


Fig. 4. Robot alignment registration chain. Solid lines mark known transformations, dashed lines mark computed transformations. An arrow from coordinate system a to coordinate system b denotes the transformation T_b^a .

is limited. Furthermore, only one fluoroscopic X-ray image can be used, since there is no tracking of the C-arm pose. Finally, the C-arm imaging system exhibits orientation-dependent distortions and internal imaging parameters variations. To cope with these challenges, we have developed a novel model-based approach for robust and accurate localization of the drill guide target and nail holes and for the registration of their axes.

We model the fluoroscopic camera as a pin-hole camera with distortion, as this has been shown to be an appropriate approximation of the X-ray imaging process [8], [20], [21]. In previous work [21], we describe a robust automatic C-arm calibration algorithm that includes fiducial localization, distortion correction and camera calibration. The algorithm computes the distortion correction and camera calibration parameters from a fluoroscopic X-ray image in three steps. First, it locates the fiducials' projections and pairs them with their spatial location. Next, it computes the distortion correction parameters, and then computes the calibration parameters. Accurate and robust localization of the fiducials and their pattern is the most important step, since all parameters critically depend on it. Our experiments show that submillimetric accuracy for the combined dewarping and camera calibration is achievable even when only 60% of the fiducials are detected [21].

The nail is modeled as a planar object with two circular holes. This is a good approximation since the nail's distance from the camera focal point is 450–700 mm and the nail diameter is 10–15 mm.

To align the robot so that the drill guide axes coincide with the nail hole axes we compute the transformation chain shown in Fig. 4¹:

$$T_{base}^{goal} = T_{base}^{tip} T_{tip}^{pattern} (T_{camera}^{pattern})^{-1} T_{camera}^{nail} T_{nail}^{goal} \quad (1)$$

¹Throughout the paper, we use the following notation conventions: the spatial coordinates of a point $P = (x, y, z)$ with respect to coordinate system a are denoted by P_a . To transform the coordinates of point P with respect to coordinate system a to coordinate system b , we apply the transformation $T_b^a(P_a) = P_b$. Transformations between coordinate systems are concatenated in right to left order: $T_c^a = T_c^b T_b^a$. The inverse transformation of T_b^a is $T_a^b = (T_b^a)^{-1}$.

where T_{base}^{tip} and $T_{tip}^{pattern}$ are known from design, $T_{camera}^{pattern}$ and T_{camera}^{nail} are computed from the C-arm internal camera parameters and the fluoroscopic image, and T_{nail}^{goal} is computed from the previous two transformations.

Table I shows the registration algorithm. The first step, C-arm distortion correction and calibration, is described in [21]. Steps 2 and 3, drill guide and nail hole identification, and drill guide, nail and goal pose estimation will be described in detail next.

IV. DRILL GUIDE AND NAIL HOLE IDENTIFICATION

A. Drill Guide Identification

Drill guide identification is performed by first detecting the circular fiducials in the image and then finding the correct correspondence with their 3-D model. The key issues are handling partial occlusions and missing fiducials, and minimizing positional inaccuracies.

The target fiducials are detected in two steps: 1) localization and 2) circle fitting. Localization is performed using a modified circle Hough transform [22] and a model-based analysis of the transform accumulator. Since the circular fiducials are darker than the image background, the Hough transform voting scheme is constrained so that edge pixels will only cast their vote if the vector connecting them to the hypothesized circle center is in the opposite direction of the gradient at the edge location. The contents of the transform accumulator are examined to identify the $k > 28$ circles which received the most votes. Considering a few more candidate circles is necessary since the accumulator may contain multiple peaks for the same fiducial (these are higher than the peaks for other fiducials). The algorithm then computes the average radius and number of votes of the five circles with the most votes and selects all circles whose radius is within ± 2 pixels of the average radius and which have received more than half of the average votes. These circles, with very high probability, belong to the target.

The selected set of circles may contain overlapping circles, which result from either multiple responses for the same fiducial or from fiducial overlap. In our imaging setup, there are at most two overlapping fiducials. Thus, for each set of overlapping circles, the algorithm only retains the two circles with the highest number of votes. These pairs of overlapping circles correspond either to two overlapping fiducials or to a single fiducial. When the overlap area between the pair of circles is larger than a threshold (i.e., 60%) of the circle's area, it is considered as a single circle; otherwise it is considered as two circles. Circle fitting is performed using the Random Sample Consensus (RANSAC) paradigm [23]. For each circle, the algorithm collects all edge elements contained in its circumscribing square and fits a circle to them. This resolves the accuracy limitations imposed by the discrete nature of the Hough transform.

The correspondence between the detected fiducials and their 3-D model is computed using homographies [24]. Correctly pairing the detected fiducials and the 3-D model fiducials is difficult, as there are always missing fiducials which are occluded by the nail. To overcome these problems, we use the geometry

TABLE I
REGISTRATION ALGORITHM: OVERVIEW

<i>Input:</i> fluoroscopic X-ray images, robot kinematics model
1. <i>Distortion correction and calibration of C-arm fluoroscope:</i> Compute an image dewarp map and camera internal parameters
2. <i>Drill guide and nail hole identification:</i> <ol style="list-style-type: none"> 1. <i>Drill guide identification:</i> First, identify the drill guide fiducial location by finding the target fiducials and fitting circles to determine their centers. Then, establish the correspondence between the fiducials and their 3D model using homographies. 2. <i>Nail hole identification:</i> Locate the nail's longitudinal contours and then locate the nail holes from their expected position with respect to the contours.
3. <i>Drill guide and nail hole pose estimation:</i> <ol style="list-style-type: none"> 1. <i>Drill guide pose estimation:</i> Minimize the projection distances between the known and expected fiducial projection coordinates. 2. <i>Nail pose estimation:</i> By direct computation for a fronto-parallel view, or by minimizing the projection distances between known and expected nail hole projections for a generic view. 3. <i>Goal pose estimation:</i> By direct computation
<i>Output:</i> rigid transformation aligning the drill guide and nail holes axes.

of the drill guide target: we use lines instead of points, since lines are less sensitive to partial occlusions.

Since the fiducials are distributed on two planes, the goal is to find the pair of homographies which minimizes the distance between the detected circles and the result of applying the homographies to the target fiducials. The pair of homographies is computed in three steps:

- 1) Find line with maximal support (either long or short target axis); the other axis is nearly perpendicular to the one found.
- 2) Find all lines that contain two spheres and are nearly perpendicular (parallel) to the long axis. Sort them according to their mean projection onto the long (short) axis. The next step requires that at least two lines per target plane were identified. This means that according to the target design for the long axis there are 4–7 lines and for the short axis 4–5 lines. If more than the maximal number of lines are detected then the identification step has failed.
- 3) Go over all $\binom{7}{k}, \binom{5}{j}, 4 \leq k \leq 7, 4 \leq j \leq 5$ line pairing options. For each pairing compute the two homographies corresponding to the target planes using the direct linear transformation method [24]. Each pairing is ranked according to the number of target-image point matches and the sum of distances. We transform all target points and pair them with the closest image point which is at most $2r$ pixels away, where r is the average radius of the detected circles. The best pairing is the one which maximizes the number of matches. When there is more than one such pairing, we choose the one which minimizes the total distance between transformed target points and their matched image points.

These steps produce the target-image correspondences, which may contain pairings between several target points and a single image point. This occurs when the target spheres overlap in the image and only one is detected. All such multiple pairings are discarded. Finally, a visual validation is performed by overlaying on the original fluoroscopic X-ray image the detected circles and the paired target spheres. Fig. 5(a)–(e) illustrates drill

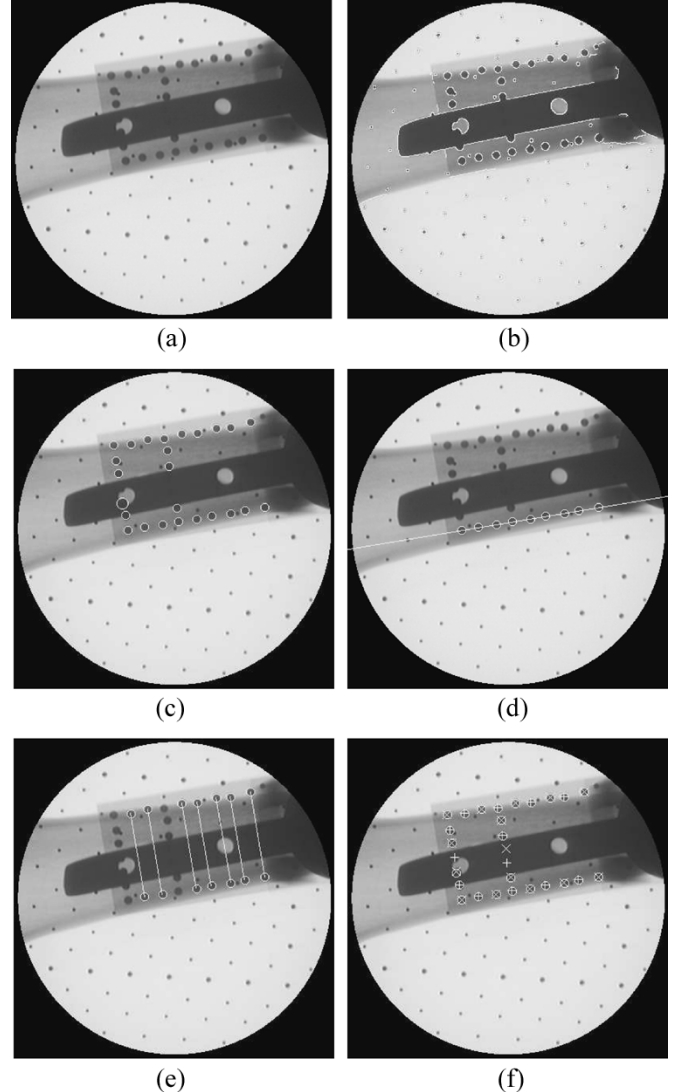


Fig. 5. Drill guide target identification from fluoroscopic X-ray image: (a) image after distortion corrected; (b) edge detection; (c) detected fiducials; (d) line with maximal support; (e) lines supported by two fiducials; (f) detected fiducials (white circles) and their associated model planes (+ and ×).

guide target detection and identification. Fig. 5(f) is the image for visual validation.

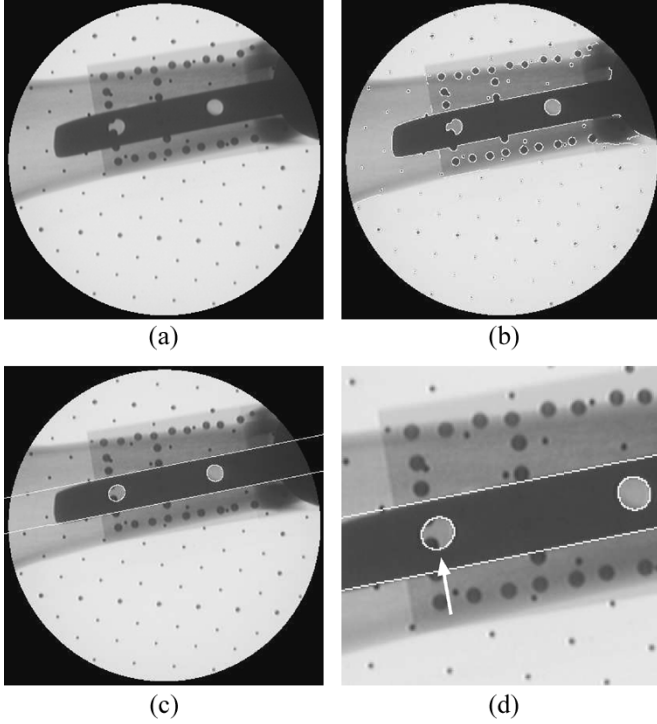


Fig. 6. Nail hole detection from fluoroscopic X-ray image: (a) image after distortion correction; (b) result of edge detection overlaid on distortion corrected image; (c) nail's longitudinal contour and detected ellipses; (d) detail of the detected nail holes; the arrow indicates occlusions due to drill guide spheres.

B. Nail Hole Identification

The location of the distal locking nail holes in the fluoroscopic X-ray image is determined by first locating the nail's longitudinal contour and then locating its holes from their expected position with respect to the contour, as shown in Fig. 6.

To locate the nail longitudinal contours, we use a 3-D Hough transform in which the nail is modeled as a band consisting of two parallel lines with a known distance between them. The Hough transform voting scheme is constrained so that pixels which are on parallel lines will only cast their vote if the gray level values between them are lower than the gray level values outside the band.

The search for the nail holes is then performed on the pixels contained between the nail's contours. The algorithm sweeps a parallelepiped window whose sizes are equal to the nail width along the nail's medial axis. The edges found between the nail's contours correspond to the nail holes, the drill guide target or the C-arm calibration target contours, as illustrated in Fig. 6(b). The two locations containing the maximal number of edge elements correspond to the distal locking nail holes. The algorithm then fits ellipses to the edge data at these locations.

To eliminate outliers (i.e., drill guide target or calibration target), we evaluated two approaches: 1) the RANSAC approach, and; 2) a model-based approach. In the RANSAC approach, subsets of five pixels are randomly chosen and the ellipse parameters are estimated using a generic conic fitting solution [25]. For each such estimate, the largest consensus set is found and is used as input for a least squares estimation

procedure. Edge elements are incorporated into the consensus set only if their geometric distance from the ellipse is below a predefined threshold. In the model-based approach, only edge elements which belong to the convex hull of the set of elements are used. This is because ellipses are convex shapes and because the nail is opaque, so outlying edges can only be present in the interior of the ellipse. The final ellipse parameters are computed in both cases using nonlinear geometric least squares optimization (Downhill-Simplex) with the initial parameters obtained from an algebraic least squares estimate [26]. Fig. 6 shows an example of the nail hole identification using the model-based approach.

Experimentation with both approaches showed the superiority of the model-based approach. The RANSAC approach failed occasionally due to the threshold value for incorporation into the consensus set. The final validation and confirmation of the ellipse fitting is done by the surgeon from visual inspection.

V. DRILL GUIDE AND NAIL POSE ESTIMATION

Estimating the desired robot pose requires the estimation of the drill guide and nail poses in the camera coordinate system.

The desired robot pose is

$$\hat{T}_{base}^{tip} = T_{base}^{goal} \left(T_{tip}^{pattern} \right)^{-1}$$

where T_{base}^{goal} is as in (1)

$$T_{base}^{goal} = T_{base}^{tip} T_{tip}^{pattern} \left(T_{camera}^{pattern} \right)^{-1} T_{camera}^{nail} T_{nail}^{goal}.$$

This transformation chain consists of two known transformations, $T_{tip}^{pattern}$, known from design, and T_{base}^{tip} , the current robot pose obtained from the robot controller, and three unknown transformations $T_{camera}^{pattern}$, drill guide pose, T_{camera}^{nail} , nail pose, and T_{nail}^{goal} , goal pose. We describe how to compute each next.

A. Drill Guide Pose Estimation

The drill guide pose is computed by nonlinear minimization of the projection distances between the known fiducial projection coordinates (x_i, y_i) and the expected ones (\hat{x}_i, \hat{y}_i)

$$\mathbf{v} = \arg \min_{\mathbf{v}} 0.5 \left(\sum_{i=1}^n (x_i - \hat{x}_i(\mathbf{v}))^2 + (y_i - \hat{y}_i(\mathbf{v}))^2 \right)$$

where $\mathbf{v} = [\mathbf{t}, \mathbf{r}]$ is the rigid transformation parametrization, with \mathbf{t} a translation vector and \mathbf{r} either Euler angles or the vector part of a unit quaternion. The nonlinear minimization is performed with the Levenberg–Marquardt method as described in [27].

B. Nail Pose Estimation

Nail pose is determined from a single fluoroscopic X-ray image. We consider two alternatives, depending on what is assumed about the viewing direction of the C-arm: 1) an FP view or 2) general view (no assumption). The first option requires the X-ray technician to acquire a few fluoroscopic images until the

orientation of the C-arm forms a FP setup with the nail holes. The second is generic and requires the acquisition of a single image for the whole procedure. However, it is computationally more complex and potentially less accurate.

1) *Pose Estimation From a Fronto-Parallel (FP) View:* To obtain a FP fluoroscopic X-ray image, the X-ray technician images the nail and adjusts the C-arm orientation until the elliptical holes projections become circles in the image. The orientation adjustment is based on two criteria: 1) hole circularity, and; 2) deviation angle between hole supporting plane and camera viewing direction. When the setup is a fronto parallel setup the nail holes appear in the image as circles and the angular deviation between the nail hole's supporting plane normal and the camera viewing direction is zero.

We define the distance from the FP setup as a function of the hole circularity, the aspect ratio of the ellipse which is fit to the data points, and the angular deviation between the hole's computed supporting plane normal [28], [29] and the camera's viewing direction.² This serves to guide the X-ray technician to the desired setup. We have empirically found this process to require up to six images.

Once the FP setup is achieved, the nail distance z from the camera focal point is estimated. The nail distance $z = (fd_w/d_i)$ is computed from the camera focal length f , the average diameter of the two nail holes in the image d_i and their known diameter d_w .

The nail pose in the camera coordinate system is

$$\mathbf{t} = \begin{bmatrix} \frac{z}{f}\mathbf{p}_x \\ \frac{z}{f}\mathbf{p}_y \\ z \end{bmatrix} \quad R = \begin{bmatrix} \mathbf{p}_x - \mathbf{q}_x & \mathbf{p}_y - \mathbf{q}_y & 0 \\ \mathbf{p}_y - \mathbf{q}_y & \mathbf{q}_x - \mathbf{p}_x & 0 \\ 0 & 0 & -1 \end{bmatrix}$$

where \mathbf{p} and \mathbf{q} are the centers of the two circles. The nail's X axis direction (choice of \mathbf{p} , \mathbf{q}) is set so that its angular deviation from the direction of the drill guide's X axis is minimal.

2) *Pose Estimation From a Generic View:* To determine the nail pose from a single fluoroscopic X-ray image in general orientation, we perform point based pose estimation. The nail pose is computed in three steps: 1) compute image points which correspond to known spatial points; 2) pair the corresponding image points and spatial points, and; 3) compute the nail pose, as described in Section V-A.

To compute image points which correspond to known spatial points, we observe that the imaged nail holes, modeled as circles, are projectively transformed to ellipses in the image. The goal is to find a set of points defined by the circles which are invariant under a projective transformation. In general, the intersection and bitangent points of the two circles are invariant under a projective transformation [28], [30]. In our specific case, we know that the two circles have four bitangent lines and no intersection points. The ellipses' bitangent lines are computed as described in [30].

In homogeneous coordinates the ellipses are described as

$$\mathbf{x}^T Q_1 \mathbf{x} = 0 \quad \text{and} \quad \mathbf{x}^T Q_2 \mathbf{x} = 0$$

²The computation of the supporting plane normal has two solutions yielding two angles. We display the smaller angle as we assume that the images are acquired near the FP setup.

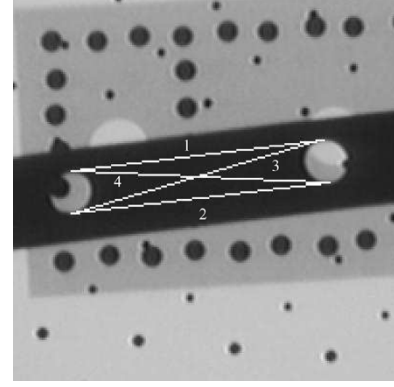


Fig. 7. Bitangents in the fluoroscopic X-ray image. The intersection point of bitangents three and four is the one used in the evaluation of the bitangent identification step.

where

$$Q_i = \begin{bmatrix} a_i & 0.5b_i & 0.5d_i \\ 0.5b_i & c_i & 0.5e_i \\ 0.5d_i & 0.5e_i & f_i \end{bmatrix}$$

and $[a_i, b_i, c_i, d_i, e_i, f_i]$ are the coefficients of the ellipse's quadratic form.

The normal to Q_1 is $\mathbf{n}_1 = 2Q_1\mathbf{x}$ and the tangent line at \mathbf{x}_1 is the set of points \mathbf{R} which are orthogonal to \mathbf{n}_1

$$\begin{aligned} \mathbf{n}_1^T \mathbf{r} &= 0 \\ 2\mathbf{x}_1^T Q_1 \mathbf{r} &= 0 \end{aligned}$$

where $\mathbf{r} \in \mathbf{R}$.

Let $\mathbf{l}_1^T = \mathbf{x}_1^T Q_1$. Then $\mathbf{l}_1^T \mathbf{r} = 0$ is a line. Using the duality of points and lines, we can view the line \mathbf{l}_1^T as a point on the ellipse Q_1^{-1}

$$\mathbf{l}_1^T Q_1^{-1} \mathbf{l}_1 = \mathbf{x}_1^T Q_1 Q_1^{-1} Q_1 \mathbf{x}_1 = 0. \quad (2)$$

Similarly, for the second ellipse

$$\mathbf{l}_2^T Q_2^{-1} \mathbf{l}_2 = 0. \quad (3)$$

The bitangent \mathbf{l} of Q_1 , Q_2 satisfies both (2) and (3). Hence, the line \mathbf{l} corresponds to the intersections of the ellipses Q_1^{-1} and Q_2^{-1} , the four solutions to the two polynomial equations defined by the ellipses.

To pair corresponding image points and spatial points, we note that the perspective transformation does not change the order of the tangency points around the ellipse/circle. Thus, there are four possible matches, one for each pairwise combination of bitangent lines. The bitangents are enumerated in counter-clockwise order according to the bitangent points on the first circle, as illustrated in Fig. 7. Since the nail is modeled as a planar object with two circular holes, every prospective match induces a homography. The matches are then ranked using this homography, which is computed using the four bitangent points associated with the first circle. A match is ranked by the distance between the intersection point of bitangents three and four in the image and the mapping of their intersection point from the world

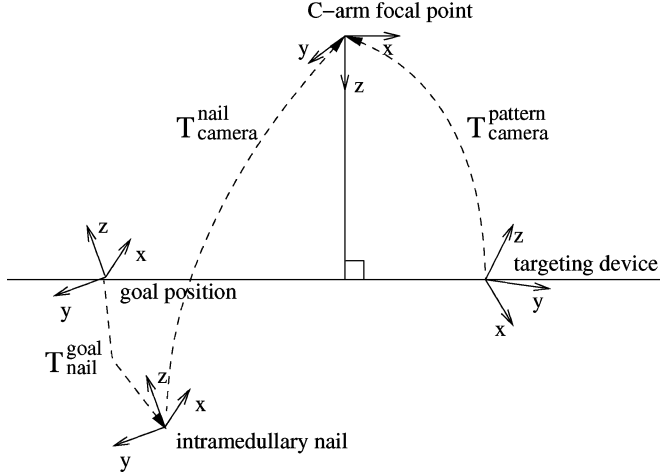


Fig. 8. The goal pose is defined by the drill guide target and nail poses in the camera coordinate system.

plane to the image plane. The match with the minimal distance is the correct one.

The correct match yields thirteen pairs of points on the nail hole plane and the image plane, corresponding to the eight bitangent points and the five intersection points of the bitangents. We also add the two image coordinates of the nail hole centers, which are computed as described in [29]. In total, fifteen point matches for use in the pose estimation.

C. Goal Pose Estimation

The goal pose, corresponding to the final pose of the drill guide target, is computed from the drill guide target pose, $T_{\text{camera}}^{\text{pattern}}$, and the nail pose, $T_{\text{camera}}^{\text{nail}}$. Note that the orientation of the goal pose is the same as that of the nail. The location of the goal pose is defined as the intersection point of the nail pose z axis with a plane which is parallel to the camera xy plane and at the same distance as the drill guide target from the camera origin (Fig. 8).

Let the transformation $T_b^a = [R_b^a; \mathbf{t}_b^a]$ be defined by a 3×3 rotation matrix R_b^a and a 3×1 translation vector \mathbf{t}_b^a . Then

$$\begin{aligned} \mathbf{t}(3)_{\text{camera}}^{\text{pattern}} &= \mathbf{t}(3)_{\text{camera}}^{\text{nail}} + \lambda R(3, 3)_{\text{camera}}^{\text{nail}} \\ \text{giving } \lambda &= \frac{\mathbf{t}(3)_{\text{camera}}^{\text{pattern}} - \mathbf{t}(3)_{\text{camera}}^{\text{nail}}}{R(3, 3)_{\text{camera}}^{\text{nail}}} \end{aligned}$$

which yields the desired translation

$$\mathbf{t}_{\text{nail}}^{\text{goal}} = \lambda \begin{bmatrix} R(1, 3)_{\text{camera}}^{\text{nail}} \\ R(2, 3)_{\text{camera}}^{\text{nail}} \\ R(3, 3)_{\text{camera}}^{\text{nail}} \end{bmatrix}.$$

Note that $R(3, 3)_{\text{camera}}^{\text{nail}}$ will never be zero since the nail z axis is perpendicular to the hole plane, for otherwise the nail holes would not be visible in the image.

VI. EXPERIMENTAL RESULTS

We designed and conducted experiments to quantify the accuracy and robustness of the proposed system. The accuracy de-

pends on the image processing and point-based estimation algorithms, and on the accuracy of the MARS robot. Specifically, we conducted the following five experiments.

- 1) Evaluation of the image processing algorithms.
- 2) Evaluation of the point-based pose estimation algorithms.
- 3) Evaluation of the sensitivity of the two nail pose estimation methods.
- 4) Assessment of variability of the robot reference pose.
- 5) Whole-system accuracy assessment.

All images were acquired with a 9" BV29 C-arm (Phillips, The Netherlands). They were 768×576 pixels, 8-bit gray-scale. All algorithms were implemented in C++ and ran on a 2.4 GHz, 1 GB RAM PC running Windows XP. Processing times were 5–10 s/image.

A. Image Processing Algorithm Evaluation

To test the robustness of the drill guide and nail hole identification, we manually placed the robot and C-arm in random positions. We then acquired 78 fluoroscopic X-ray images. The drill guide and nail holes were correctly identified in 61 images. There were six failures due to problems with the drill guide target detection, because not enough target fiducials were found. For 11 images, the procedure failed due to substantial nail occlusion of the target. These failures can be corrected, as the operator can manually orient the robot so that more of the fiducials are visible. The software automatically detected all failures and produced no false positives: the drill guide and nail holes were always detected correctly.

B. Point-Based Pose Estimation Evaluation

Point-based pose estimation is a problem which has been thoroughly studied in Computer Vision. We explored solutions to this problem with three factors in mind, ordered according to their importance: 1) achieve the highest accuracy possible; 2) deal with noisy input data without any outliers, and; 3) efficient computation, within several seconds. Since no solution has been shown to always be superior, we implemented and evaluated the following four point-based pose estimation algorithms.

- 1) Direct linear transform (DLT) [31].
- 2) Depth-based (DB) estimation [32].
- 3) Genetic Algorithm (GA).
- 4) Nonlinear (NL) optimization (Levenberg–Marquardt).

The first two algorithms, DLT and DB, do not require initialization. The GA approach requires coarse parameter bounds, which are computed from the camera internal parameters and the fact that the imaged object is between the focal point and the image plane. The NL method requires an initial guess, which is obtained from the application of the three other methods, NL-DLT, NL-DB, and NL-GA. Different rotation parameterizations (unit quaternion and Euler angles) did not affect the results of the NL method.

Table II summarizes the results of pose estimation on 61 input images. For each image automatic drill guide detection was performed and its output was used as input for pose estimation. The number of input points varied between 20 to 28. To compare the algorithms, we chose the NL method as a reference, as it had the smallest 2-D and 3-D errors in all experiments.

TABLE II
COMPARISON OF POSE ESTIMATION ALGORITHMS (MEAN ERRORS AND STANDARD DEVIATIONS COMPUTED FOR 61 DATA SETS). TIMES REPORTED AS 0.00 s INDICATE THAT THE COMPUTATION TOOK LESS THAN 0.005 s

Algorithm	Time (sec) mean std	Error (mm)		Deviation from NL-GA (mm,degrees)					
		mean std		mean std					
		2D	3D	x	y	z	θ_x	θ_y	θ_z
DLT	0.00	409.35	229.06	180.68	140.04	48.16	1.62	0.97	0.07
	0.00	184.86	95.86	78.32	61.39	49.74	1.64	0.89	0.14
DB	7.49	0.26	0.16	0.16	0.11	4.76	0.16	0.26	0.01
	4.44	0.34	0.22	0.31	0.13	6.27	0.23	0.48	0.01
GA	4.24	1.34	0.87	0.37	1.07	4.66	1.02	0.88	2.35
	0.16	2.79	1.85	0.70	2.43	10.79	1.90	1.82	5.34
NL-DLT	0.00	0.09	0.06	0.00	0.00	0.00	0.00	0.00	0.00
	0.00	0.10	0.06	0.00	0.00	0.00	0.00	0.00	0.00
NL-DB	7.54	0.09	0.06	0.00	0.00	0.00	0.00	0.00	0.00
	4.47	0.10	0.06	0.00	0.00	0.00	0.00	0.00	0.00
NL-GA	4.32	0.09	0.06	0.00	0.00	0.00	0.00	0.00	0.00
	0.22	0.10	0.06	0.00	0.00	0.00	0.00	0.00	0.00

The NL method gave the most accurate results and converged to the same minimum no matter which initialization method was used. It is followed by DB, GA and finally DLT. As expected, the DLT method gave the worst results since it ignored the constraints on the rotation matrix in addition to the noisy input. The GA method did worse than the DB method most likely because of early termination with suboptimal results. Both the GA and DB methods are not accurate enough for this application, as they are not sensitive enough to changes in the distance along the viewing direction. This is most evident in the DB method where the 2-D and 3-D errors are below 0.5 mm, yet the difference along the viewing direction from the reference pose may be up to 10 mm.

The NL-DLT method and DLT method tie for the best running time (≤ 5 ms). The GA method's running times are consistent and are similar for all inputs. The DB method gave the worst running times and a large standard deviation. This is because one of its steps is a Singular Value Decomposition of a matrix whose number of rows is a cubic function of the number of input points (20–28). The NL-DLT gives the best results both in accuracy and time, no matter what initialization method is used. This means that in practice the optimized function does not have local minima near the global one. Had this not been the case we would expect that: 1) the NL-GA method would give the best accuracy results, as it is the only method which uses robust initialization, and 2) there would be cases in which the NL-DLT method would fail, as it initializes the NL stage far from the global minimum.

We also evaluated the sensitivity of the NL-DLT method by performing a Monte Carlo simulation. Fig. 9 summarizes the results of running the NL-DLT method on 61 input images with varying amounts of noise added to the detected fiducial locations. For each image, automatic drill guide detection was performed and its output was used as the input for the NL-DLT method. We then added zero mean Gaussian noise to the detected fiducials and evaluated the parameter deviation with regard to the results obtained using the original data. The Gaussian standard deviation was varied in the range [0.5–2.5]

pixels (maximal standard deviation size is approximately half the fiducial radius).

As with the evaluation of the pose estimation algorithms, we observed again that the method is most sensitive along the viewing direction (z axis). We also noted that the NL-DLT method is robust at the expected noise levels (i.e., errors in fiducial detection are smaller than half the fiducial radius), making it suitable for our application.

C. Nail Pose Estimation Sensitivity

To evaluate the sensitivity of the two algorithms described in Section V-B, we performed the following Monte Carlo simulation. First, we ran the nail hole detection step on the 17 FP setup images. Then, we added zero mean Gaussian noise to the nail hole edge elements and re-estimated the ellipse parameters. The new ellipses were used as input to both algorithms, and we measured the deviation from their original results (Fig. 10). The Gaussian standard deviation varied in the range [0.5–2.5] pixels. The maximal standard deviation was chosen as 2.5 pixels, as at this noise level the ellipse fit is already visibly erroneous. Fig. 11 shows a representative image.

We conclude that the method that assumes a FP setup is more stable. This is because it only uses the ellipse centers in the computation of the nail pose, while the method that does not assume a FP setup uses the ellipse bitangents which are dependent on all the ellipse parameters.

D. Robot Reference Pose Evaluation

The reference robot pose is defined as the pose in which two rods (4 mm diameter) pass through the drill guide and nail holes (5 mm diameter), Fig. 2(b). In this pose, successful locking is guaranteed.

Since the reference pose is not unique, as there is a clearance between the rod and the nail hole, we must define a comparison measure for the different poses. Direct comparison of the Euler angles and translations does not reflect relevant errors for the task at hand. Instead, we consider the angular deviation of the drill guide axes and the distance between axes entry and exit

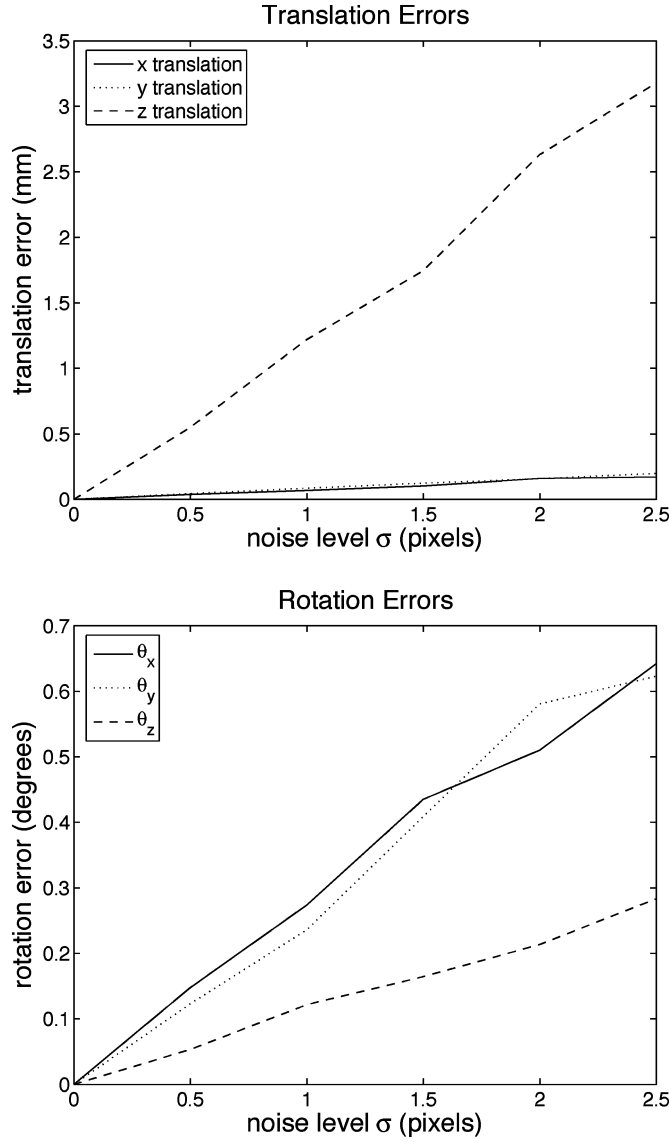


Fig. 9. Deviation of the pose parameter values using the NL-DLT algorithm with varying amounts of noise (zero mean Gaussian) added to the detected image fiducial centers, mean errors computed for 61 data sets. Nominal pose parameter $\{x, y, z, \theta_x, \theta_y, \theta_z\}$ values were in the following ranges: $\{[-16.47, 28.33], [-19.77, 24.69], [605.46, 640.38], [-10.11, 11.66], [-5.40, 9.66], [-21.11, 39.41]\}$. Translation units are mm and rotation units degrees.

points. This distance is defined as the in-plane distance between the intersection points of the axes and two planes located at 100 mm and 120 mm from the robot base (the nail is located between these planes). Fig. 12 illustrates this setup.

To assess the possible variability of the reference pose, we manually placed the robot in 18 different poses in which the two rods passed through the drill guide and nail holes. We then compared all the transformations to each other and found an angular variability in the range of 0° – 0.9° and a translational variability in the entry and exit points in the range of 0–3.9 mm.

E. Whole System Evaluation

To quantify the accuracy of the whole system, we conducted the following experiment in the setup shown in Fig. 2(a). The

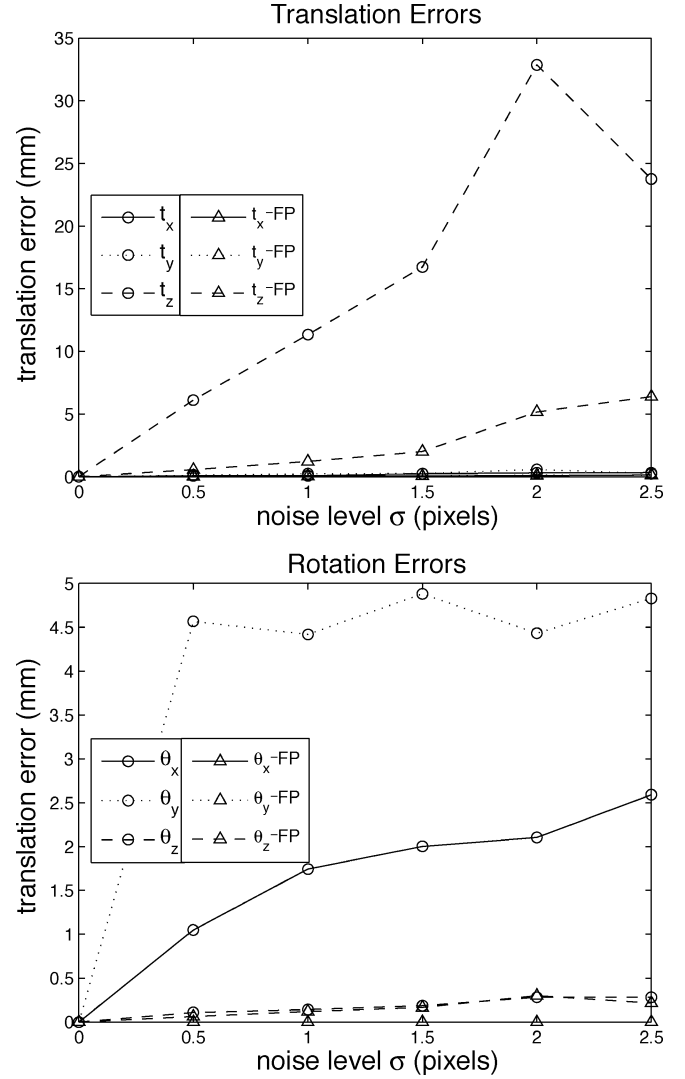


Fig. 10. Deviation of both nail pose estimation algorithms, assuming FP and without this assumption, for different noise levels (zero mean Gaussian) that are added to the nail hole edge elements.

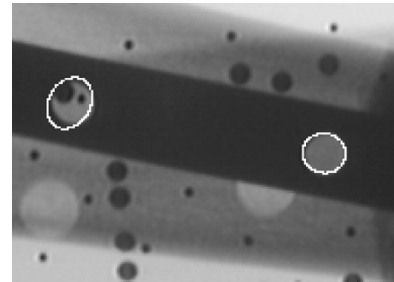


Fig. 11. The resulting ellipses when zero mean Gaussian noise with a 2.5 pixel standard deviation is added to the original nail hole edges. The erroneous result is clearly visible and can be readily rejected by the X-ray technician or surgeon.

robot was first placed in a reference pose. Next, under the guidance of our software, the C-arm was oriented to a FP view with respect to the nail holes. We then placed the robot in 17 random poses, acquired fluoroscopic X-ray images, and computed the robot alignment for each pose. In all experiments, three to six images were sufficient to achieve a fronto parallel setup. Drill guide target and nail holes were correctly detected in all images.

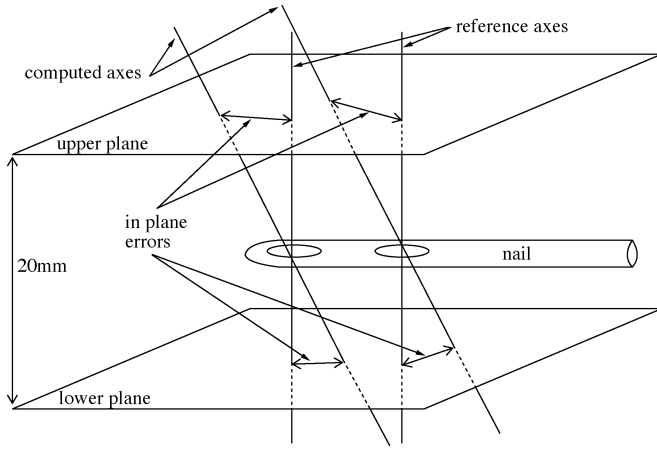


Fig. 12. The in-plane distance between computed axes intersection points and reference axes intersection points.

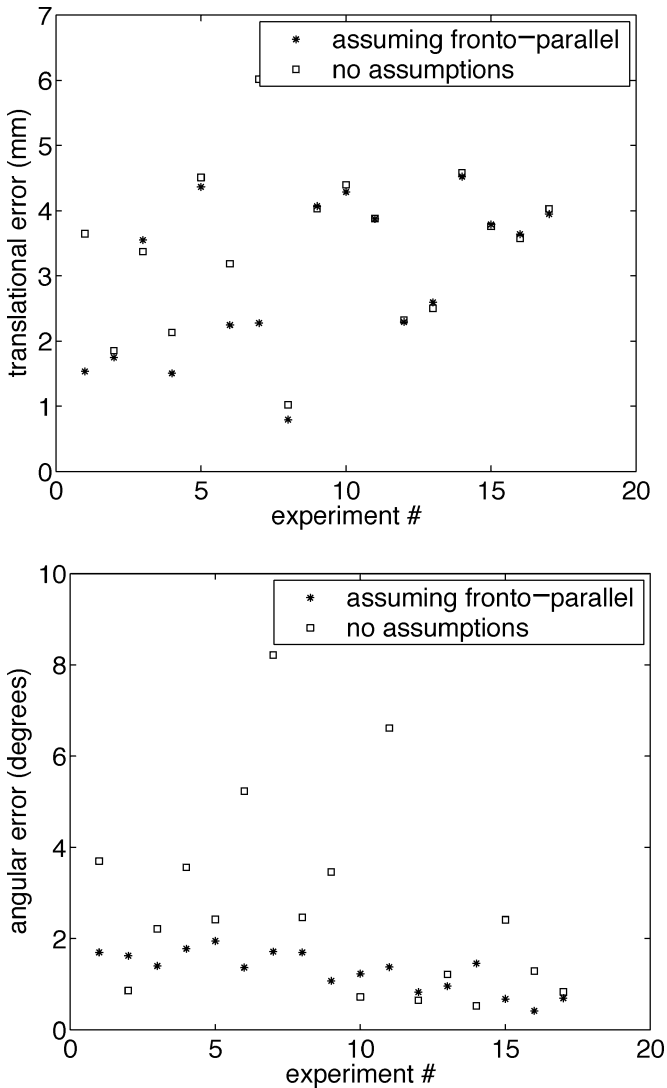


Fig. 13. Angular and translational errors relative to the reference pose.

We evaluated both pose estimation with FP viewing (Section V-B1) and with generic viewing (Section V-B2). In both, we computed the robot pose and compared it to the reference pose.

For the FP setup, we obtained a mean angular error of 1.3° (std = 0.4°) between drill guide axes, and a mean 3.0 mm error (std = 1.1 mm) in the entry and exit points. For the generic setup, we obtained a mean angular error of 2.7° (std = 2.1°) between drill guide axes, and a mean 3.4 mm error (std = 1.2 mm) in the entry and exit points. Fig. 13 summarizes the results for all 17 experiments. The translational error is either comparable between approaches or smaller when using the FP assumption. The rotational error is smaller in the FP setup and has a smaller variability.

We conclude that the FP setup approach is more robust and accurate. In both, the nail holes are detected and ellipses fit to them. In the FP approach, we measure the deviation from the FP setup by displaying the ellipse aspect ratio and the angular deviation between the circle supporting plane normal and the camera's viewing direction. This computation is done separately for each of the ellipses and in the case of the aspect ratio, only two of the ellipse parameters are used in the computation. In the generic approach, all ellipse parameters from both ellipses are used in a single computation, making the computation more sensitive to parameter errors from both ellipses.

VII. CONCLUSIONS

We have presented a novel image-guided robot-based system to assist orthopedic surgeons in performing distal locking of long bone intramedullary nails. The system uses a miniature robot fitted with a drill guide that provides rigid mechanical guidance for hand-held drilling of the distal screws' pilot holes. The robot is rigidly attached to the distal femur or the intramedullary nail head and is automatically positioned so that the drill guide and nail distal locking axes coincide using a single fluoroscopic X-ray image. In contrast with existing medical robotics systems, our system is unobstructive, less invasive, less expensive, and does not require leg immobilization or closed-loop real-time tracking.

The key computational task is automatic accurate and robust rigid registration between the robot-mounted drill guide axes and the intramedullary nail hole axes based on a single fluoroscopic X-ray image. We have presented an open-loop calibrated fluoroscopic guidance algorithm that performs the registration by automatically locating the drill guide and the nail holes in the fluoroscopic X-ray image and computing their relative pose. Our experiments show that fronto-parallel viewing setup, in which the X-ray technician images the nail and adjusts the C-arm orientation with guidance from our software until the elliptical nail holes projections become perfect circles, yields the best accuracy and stability. The mean error of 3.0 mm (std = 1.1 mm) between the entry and exit drill point is adequate for successfully locking the nail.

Open issues that remain to be explored include the evaluation of the bone and the nail head attachment rigidity, sensitivity analysis, and more *in vitro* and cadaver validation and accuracy experiments. Previous work on spine fixation [19] and our limited experience with the intramedullary nail indicates that, unless the bone is osteoporotic, the fixation concept is rigid and viable. These issues are currently being addressed by Mazor Surgical Technologies Ltd. (Caesarea, Israel), the

manufacturer of MARS, who is currently developing a module for intramedullary nail distal locking based on the concepts described in this paper.

ACKNOWLEDGMENT

The authors would like to thank Mazor Surgical Technologies Ltd. for the use of the MARS robot.

REFERENCES

- [1] L. P. Nolte and R. Ganz, Eds., *Computer Assisted Orthopaedic Surgery (CAOS)*. Kirkland, WA: Hogrefe and Huber, 1999.
- [2] R. J. Brumback, "The rationales of interlocking nailing of the femur, tibia, and humerus: an overview," *Clin. Orthopaedics Related Res.*, vol. 324, pp. 292–320, 1996.
- [3] S. Skjeldal and S. Backe, "Interlocking medullary nails—radiation doses in distal targeting," *Arch. Orthopaedic Trauma Surg.*, vol. 106, pp. 179–181, 1987.
- [4] M. Shoham, M. Burman, E. Zehavi, L. Joskowicz, E. Batkalin, and Y. Kunicher, "Bone-mounted miniature robot for surgical procedures: concept and clinical applications," *IEEE Trans. Robot. Automat.*, vol. 19, no. 5, pp. 893–901, Oct. 2003.
- [5] L. Joskowicz, C. Milgrom, M. Shoham, Z. Yaniv, and A. Simkin, "A robot-assisted system for long bone intramedullary distal locking: concept and preliminary results," in *Proc. Computer Assisted Radiology and Surgery*, 2003, pp. 485–491.
- [6] T. Ohe *et al.*, "Stereo fluoroscopy-assisted distal interlocking of intramedullary nails," *J. Orthopaedic Trauma*, vol. 11, no. 4, pp. 300–303, 1997.
- [7] C. Krettek *et al.*, "A mechanical distal aiming device for distal locking in femoral nails," *Clin. Orthopaedics*, vol. 384, pp. 267–275, 1999.
- [8] R. Hofstetter, M. Slomczykowski, M. Sati, and L. P. Nolte, "Fluoroscopic as an imaging means for computer-assisted surgical navigation," *Comput. Aided Surg.*, vol. 4, no. 2, pp. 65–76, 1999.
- [9] L. Joskowicz, "Fluoroscopy-based navigation in computer-aided orthopaedic surgery," presented at the *IFAC Conf. Mechatronic Systems*, Darmstadt, Germany, 2000.
- [10] E. J. Hazan and L. Joskowicz, "Computer-assisted image-guided intramedullary nailing of femoral shaft fractures," *Tech. Orthopaedics*, vol. 18, no. 2, pp. 130–140, 2003.
- [11] S. Malek *et al.*, "Validations of computer-assisted orthopaedic surgical system for insertion of distal locking screws for intramedullary nails," in *Proc. Computer-Assisted Radiology and Surgery*, 2004, pp. 614–619.
- [12] K. Cleary and C. Nguyen, "State of the art in surgical robotics: clinical applications and technology challenges," *Comput. Aided Surg.*, vol. 6, no. 6, pp. 312–328, 2001.
- [13] R. H. Taylor and D. Stoianovici, "Medical robotics in computer-integrated surgery," *IEEE Trans. Robot. Automat.*, vol. 19, no. 5, pp. 765–781, Oct. 2003.
- [14] A. Bzostek *et al.*, "An automated system for precise percutaneous access of the renal collecting system," in *Lecture Notes in Computer Science*, ser. . Berlin, Germany: Springer-Verlag, 1997, vol. 1205, Proc. CVRMed/MRCAS, pp. 299–308.
- [15] J. Yao *et al.*, "A c-arm fluoroscopy-guided progressive cut refinement strategy using a surgical robot," *Comput. Aided Surg.*, vol. 5, no. 6, pp. 373–390, 2000.
- [16] A. Patriciu *et al.*, "Motion-based robotic instrument targeting under c-arm fluoroscopy," in *Proc. Medical Image Computing and Computer Assisted Intervention*, 2000, pp. 988–998.
- [17] N. Navab *et al.*, "Visual servoing for automatic and uncalibrated needle placement for percutaneous procedures," in *Proc. Computer Vision and Pattern Recognition*, 2000, pp. 2327–2334.
- [18] G. Corral, L. Ibáñez, C. Nguyen, D. Stoianovici, N. Navab, and K. Cleary, "Robot control by fluoroscopic guidance for minimally invasive spine procedures," in *Proc. Computer-Assisted Radiology and Surgery*, 2004, pp. 509–514.
- [19] A. Wolf, M. Shoham, M. Schnider, and M. Roffman, "Feasibility study of a mini, bone-attached, robotic system for spinal operations: analysis and experiments," *Spine*, vol. 29, no. 2, pp. 220–228, 2004.
- [20] C. Brack *et al.*, "Accurate x-ray based navigation in computer-assisted orthopedic surgery," in *Proc. Computer-Assisted Radiology and Surgery*, 1998, pp. 716–722.
- [21] H. Livyatan, Z. Yaniv, and L. Joskowicz, "Robust automatic c-arm calibration for fluoroscopy-based navigation: a practical approach," in *Proc. Medical Image Computing and Computer Assisted Intervention*, 2002, pp. 60–68.
- [22] R. Jain, R. Kasturi, and B. G. Schunk, *Machine Vision*. New York: McGraw-Hill, 1995.
- [23] M. A. Fischler and R. C. Bolles, "Random sample consensus: a paradigm for model fitting with applications to image analysis and automated cartography," *Commun. ACM*, vol. 24, no. 6, pp. 381–395, 1981.
- [24] R. I. Hartley and A. Zisserman, *Multiple View Geometry in Computer Vision*. Cambridge, U.K.: Cambridge Univ. Press, 2000.
- [25] Z. Zhang, "Parameter estimation techniques: a tutorial with application to conic fitting," *Image Vis. Computing*, vol. 15, no. 1, pp. 59–76, 1997.
- [26] A. Fitzgibbon, M. Pilu, and R. B. Fisher, "Direct least square fitting of ellipses," *IEEE Trans. Pattern Anal. Machine Intell.*, vol. 21, no. 5, pp. 476–480, May 1999.
- [27] H. B. Nielsen, "Damping Parameter in Marquardt's Method," Dept. Math. Modeling, Tech. Univ. Denmark, Lyngby, Denmark, Tech. Rep. IMM-REP-1999-05, 1999.
- [28] D. Forsyth, J. L. Mundy, A. Zisserman, C. Coelho, A. Heller, and C. Rothwell, "Invariant descriptors for 3D object recognition and pose," *IEEE Trans. Pattern Anal. Machine Intell.*, vol. 13, no. 10, pp. 971–991, Oct. 1991.
- [29] K. Kanatani and W. Liu, "3D interpretation of conics and orthogonality," *CVGIP: Image Understanding*, vol. 58, no. 3, pp. 286–301, 1993.
- [30] C. A. Rothwell, A. Zisserman, C. I. Marinos, D. A. Forsyth, and J. L. Mundy, "Relative motion and pose from arbitrary plane curves," *Image Vis. Computing*, vol. 10, no. 4, pp. 250–262, 1992.
- [31] O. Faugeras, *Three-Dimensional Computer Vision: A Geometric View-Point*. Cambridge, MA: MIT Press, 1993.
- [32] A. Ansar and K. Daniilidis, "Linear pose estimation from points or lines," *IEEE Trans. Pattern Anal. Machine Intell.*, vol. 25, no. 5, pp. 578–589, May 2003.